Nuclear Inst. and Methods in Physics Research, A 939 (2019) 1–9

Contents lists available at ScienceDirect

Nuclear Inst. and Methods in Physics Research, A

journal homepage: www.elsevier.com/locate/nima

The CsI ball ancillary detector array for TIP and TIGRESS at TRIUMF

J. Williams [a,*], C. Andreoiu [a], G.C. Ball [b], N. Bernier [b,c], M. Bowry [b], S.S. Bhattacharjee [b], C. Burbadge [e], R. Caballero-Folch [b], A. Chester [b], F.H. Garcia [a], A.B. Garnsworthy [b], S.A. Gillespie [b], G. Hackman [b], R. Henderson [b], B. Jigmeddorj [e], C. Jones [f], P. Kowalski [d], R. Lafleur [e], A.D. MacLean [e], M. Morrison [d], B. Olaizola [b], Y. Saito [b,c], L. Sexton [b,f], P. Šiurytė [b,f], J. Smallcombe [b,1], K. Starosta [a,*], C.E. Svensson [e], M. Spencer [b,f], E. Timakova [b], K. Van Wieren [d], P. Voss [a,2], M. Winokan [b,f], F. Wu [a]

[a] Department of Chemistry, Simon Fraser University, Burnaby, BC V5A 1S6, Canada
[b] TRIUMF, 4004 Wesbrook Mall, Vancouver, BC V6T 2A3, Canada
[c] Department of Physics & Astronomy, University of British Columbia, Vancouver, BC V6T 1Z1, Canada
[d] Science Technical Center, Simon Fraser University, Burnaby, BC V5A 1S6, Canada
[e] Department of Physics, University of Guelph, Guelph, Ontario N1G 2W1, Canada
[f] Department of Physics, University of Surrey, Guildford, Surrey GU2 7XH, United Kingdom

ARTICLE INFO

Keywords:
Charged particle detector array
Coulomb excitation
Fusion–evaporation
Gamma-ray spectroscopy
CsI(tl) pulse shape analysis

ABSTRACT

An array of 128 CsI(Tl) charged particle detectors providing nearly 4π coverage has been developed at Simon Fraser University (SFU) and commissioned at TRIUMF, Canada's particle accelerator center. The new CsI ball array replaces a previous 24-detector array and offers improved charged particle detection efficiency and discrimination between reaction channels due to its increased angular coverage. A technical overview of the CsI ball array, as well as commissioning data including measurements of the charged particle detection efficiency, is presented.

1. Introduction

The TIGRESS Integrated Plunger device (TIP) [1] has been employed in Doppler shift lifetime measurements for the study of nuclear structure as an ancillary system for the TRIUMF–ISAC Gamma-Ray Escape Suppressed Spectrometer (TIGRESS) Compton-suppressed high purity germanium (HPGe) array [2] at TRIUMF's ISAC-II facility [3]. The TIP device facilitates nuclear lifetime measurements in the picosecond and femtosecond range using the recoil distance method (RDM) [4,5] and the Doppler-shift attenuation method (DSAM) [4], respectively.

A key component of the TIP system is the ability to identify reaction channels using an integrated array of CsI(Tl) charged particle detectors. By taking advantage of the scintillation properties of CsI(Tl), charged particles interacting with these detectors may be identified via pulse-shape analysis using the method described in Ref. [1]. A 24-element "wall" array of CsI(Tl) scintillators has successfully been deployed in multiple experiments using TIP and TIGRESS [6–8], however the charged particle detection efficiency of this array is limited by its small angular coverage.

This paper describes the development and commissioning of a new 128-element CsI(Tl) detector array, providing nearly 4π coverage in the lab frame. The increased sensitivity of this array compared to the previous "wall" array will allow for experiments utilizing increasingly exotic reaction channels and the radioactive beams available at TRIUMF.

2. The CsI ball array

2.1. Design and characteristics

The CsI ball array consists of 10 axially symmetric detector rings, covering an angular range of 3.2° to 157.65° (in comparison to the 16° to 42° covered by the 24-element wall) corresponding to 96% of the solid angle. Although arrays exist with larger angular coverage – for instance Microball which covers up to 172° [9] – the large upstream opening of the CsI ball was designed to allow operation of the array in conjunction with the TIP RDM plunger device [7] while still using all channels of the array. This design is advantageous when considering the envisioned TIP experimental program of electromagnetic transition rate measurements in nuclei far from stability, which are accessible via the exotic radioactive ion beams available at ISAC-II.

* Corresponding authors.
E-mail addresses: ejw1@sfu.ca (J. Williams), starosta@sfu.ca (K. Starosta).
[1] Present address: Department of Physics, University of Liverpool, Liverpool L69 7ZE, United Kingdom.
[2] Present address: Department of Physics, Albion College, Albion, MI, 49224, United States.

https://doi.org/10.1016/j.nima.2019.05.069
Received 18 October 2018; Received in revised form 21 May 2019; Accepted 21 May 2019
Available online 23 May 2019
0168-9002/

Table 1
Design dimensions and angular coverage of the CsI ball array. Each ring contains N_{det} detectors with a CsI(Tl) crystal of thickness Δt at a radius r defined as the distance from the center of the array to the CsI(Tl) - light guide interface. Maximum energies of stopped protons and alpha particles $E_{p,max}$ and $E_{\alpha,max}$ are calculated using the ELAST code [10]. Light guide thickness is 16.0 mm in the radial direction for all rings. For each ring of the array, $\theta_{max} = 2\theta_{avg} - \theta_{min}$.

Ring	N_{det}	CsI(Tl) Δt (mm)	r (mm)	θ_{min} (deg)	θ_{avg} (deg)	Ω_{det} (msr)	$E_{p,max}$ (MeV)	$E_{\alpha,max}$ (MeV)
0	4	5.0	92.0	3.2	8.0	36.6	35.2	136.9
1	6	2.6	57.2	9.75	17.5	84.9	24.1	93.4
2	12	2.3	57.2	25.25	33.0	76.9	22.4	86.9
3	16	2.0	57.2	40.75	48.5	79.3	20.7	80.0
4	20	1.7	57.2	56.25	64.0	76.2	18.9	73.3
5	18	1.5	57.2	71.75	79.5	92.6	17.4	67.5
6	18	1.3	57.2	87.25	95.0	93.8	16.0	62.0
7	14	1.2	57.2	102.75	111.9	132.4	15.3	59.1
8	12	1.2	57.2	121.05	130.2	127.2	15.3	59.1
9	8	1.2	57.2	139.35	148.5	130.5	15.3	59.1

Detector segmentation in the CsI ball (in terms of solid angle per detector Ω_{det}) is increased at forward angles in order to reduce the count rate per detector and avoid pileup of detector signals, which is necessary for forward detectors since products are boosted towards forward angles in the lab frame based on the center of mass motion of the beam–target system. When designing the array, the maximum possible segmentation at forward angles was achieved by maximizing the radius of the array and the number of detectors per ring. The radius of the array was constrained by the vacuum chamber dimensions (which was designed to fit within the fully populated TIGRESS array) and the number of detectors per ring was constrained by the photodiode size, which defined a minimum surface area of 10 × 10 mm for each detector in the array. Detector rings at backward angles were designed with reduced segmentation compared to the forward rings, taking advantage of the reduced count rate at backward angles obtained in the in-beam reactions studied using TIP and TIGRESS. Here the increased position resolution associated with increased segmentation is not preferable to the higher count rate per detector and the reduced number of detectors allowed by reducing the segmentation.

Design dimensions of the CsI ball array are listed in Table 1. Design drawings of the CsI ball array in the TIP reaction chamber are shown in Fig. 1.

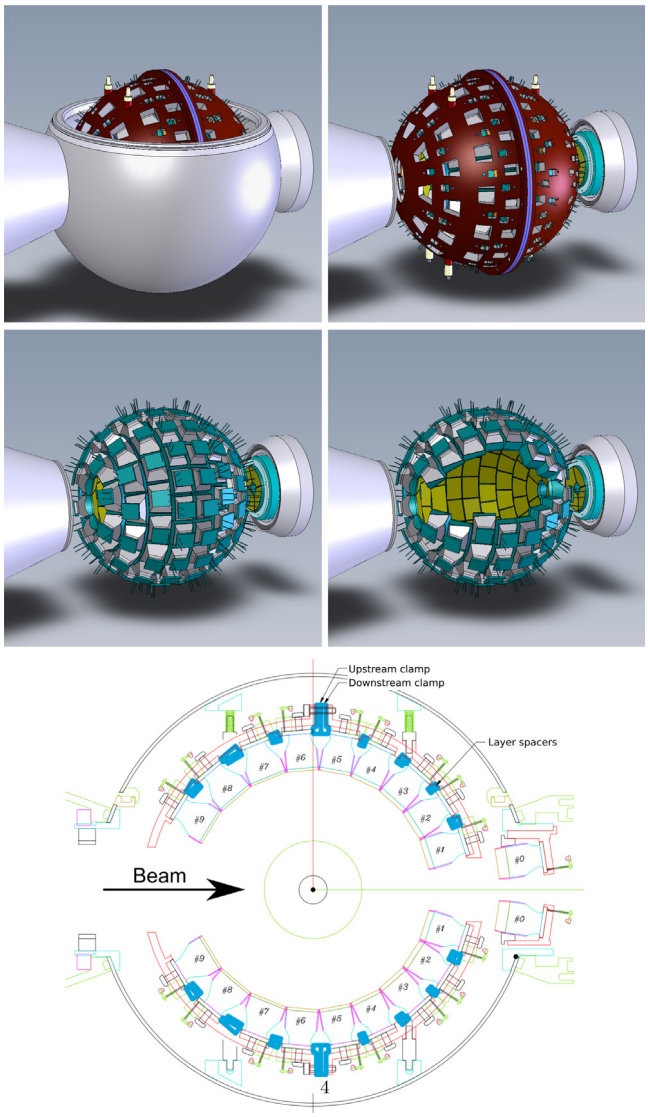

Fig. 1. Top: Breakaway view of various components of the CsI ball array within the TIP reaction chamber. A 3D printed structure supports 124 detectors organized into 9 axially symmetric rings. An additional 4 detectors are positioned further downstream. Bottom: Schematic drawing of the array inside the TIP chamber.

2.2. Detector construction and testing

Each detector in the array contains CsI(Tl) scintillator material (purchased from Hilger Crystals) with a Thallium doping concentration of ~1000 ppm as in Ref. [1] and a thickness of 1.2 to 5 mm. Each CsI(Tl) crystal is coupled to a silicon PIN diode (Hamamatsu S3590-08) via an acrylic light guide. The thickness of CsI(Tl) material used depends on the detector ring as listed in Table 1, with downstream ring detectors using thicker material to allow for stopping of charged particles boosted to high energy by the center of mass motion of the beam–target system. Detectors were constructed at Simon Fraser University (SFU) in a process adapted from Ref. [1] as detailed below:

- For each detector, a light guide was machined from UV plastic material (Saint-Gobain BC-800). The purpose of the light guide is to funnel the light produced in the CsI(Tl) scintillation process to a photodiode which produces the detector signal. The shape of the light guide is related to the specific geometry of the detector, and depends on the relative size of the CsI(Tl) crystal used with respect to the photodiode. The shape of detectors (and therefore light guides) is different for each ring in the array. A typical light guide for the CsI ball is shown in Fig. 2.
- Light guides were coupled to the CsI(Tl) crystals and photodiode using optical-grade epoxy (Saint-Gobain BC-600) at room temperature. Special care was taken to ensure the epoxy was free of bubbles, typically by placing mixed epoxy under vacuum for 1 h prior to application.
- The coupled CsI(Tl) crystal assemblies were machined to the correct thickness and geometry, matching the crystal shape to the light guide. When fly cutting the surface of the CsI(Tl) crystals, special care was taken as it was found that the choice of cutting direction impacted the brightness/dullness of the surface finish due to the orientation of the cutter with respect to the crystal structure. Additional care was taken when machining the crystal shapes as the soft CsI(Tl) material is significantly more prone to cracking and/or fracturing than the light guide plastic.
- Exterior detector faces were painted using reflective paint (Saint-Gobain BC-620), in order to increase light collection via the light guide. The paint causes light produced in the scintillation process to be reflected from the edges of the detector rather than escape it, increasing the light collected by the photodiode and therefore the signal-to-noise ratio of the detector.

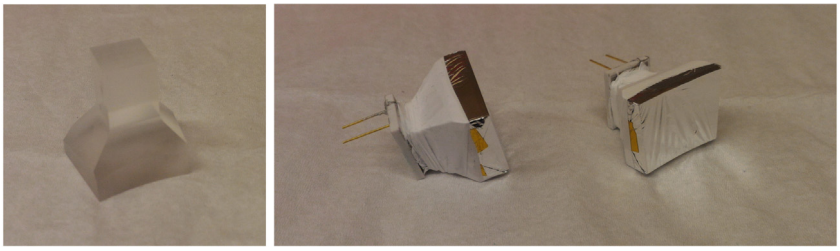

Fig. 2. Left: Machined CsI ball light guide (from array ring 8). Right: Finished individual CsI ball detectors (from array ring 7).

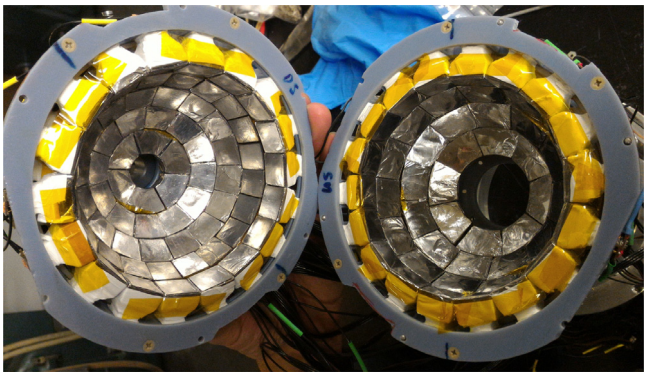

Fig. 3. Assembled CsI ball array, opened to show a view of all detectors. The front face of each detector is wrapped using a lead absorber foil as discussed in Section 3.

- Detectors were wrapped in aluminized mylar. The conductive outer surface of the mylar was connected to the ground pin of the photodiode in order to prevent charge buildup on the surface of the detector. Following mylar wrapping, the sides of the detector were wrapped in Teflon tape to prevent tearing of the mylar. The white Teflon tape also acts as a further reflective layer for any light which leaks through the reflective paint layer.

Fig. 2 shows an example of the detectors which result from the above construction process. The detectors may be further wrapped in absorber material for experiments where it is necessary to prevent scattered beam and/or heavy ions from entering the detectors — for instance, fusion–evaporation with heavy ion beams where the channel of interest is identified by detection of protons or alpha particles.

2.3. Array construction

Completed detectors were assembled into the final array using a 3D-printed frame as support. As the spatial tolerance between detector rings in the original design of the array (~ 0.5 mm between individual detectors) was found to be larger than necessary due to high precision achieved in the machining process, Kapton tape wrapping was used to increase the outer diameter of the individual detectors to fill the gaps. This was necessary as each detector in the array provides mechanical support for neighboring detectors in the same ring.

Space constraints in the TIP target chamber necessitated the closing of the array and cabling of individual detectors prior to mounting the array in the chamber. A view of the detectors assembled in their support frame is shown in Fig. 3 prior to insertion into the target chamber. Fig. 4 shows the closed array following cabling and insertion into the TIP target chamber.

2.4. Electronics

The major challenges for readout of signals from the CsI ball array were the high number of channels and poor signal-to-noise properties

Fig. 4. Cabled CsI ball array, before (top) and after (bottom) insertion into the TIP chamber.

of CsI(Tl) scintillators. To address these issues, purpose-built preamplifier boards were designed and developed at SFU. High density NIM modules were produced with 16 preamplifier channels per module, allowing the full CsI ball readout to be achieved using 8 modules. The design of the 16-fold preamplifier boards is shown in Fig. 5 alongside a finished module. CR-110 charge sensitive preamplifier modules by Cremat [11] were used. Following preamplification, a bandpass filter with bandwidth 1 kHz–12 MHz was used for noise reduction, and the resulting signal was subsequently amplified and output from the module. A detailed schematic of the signal processing stage is shown in Appendix B. Three copies of the amplified output signal are available from the rear panel of each preamplifier module, in order to facilitate additional signal processing.

Coaxial cables were fabricated to carry signals from the detectors to a feed-through in the TIP chamber, and from the external side of the feed-through to the preamp modules. Internal cables were vacuum rated. Cables and feed-throughs were designed such that individual detector signals did not share a common ground, as this was identified as a significant source of noise during the design process.

2.5. Integration with TIGRESS

The CsI ball is designed to be operated in conjunction with the TIGRESS array at ISAC-II/TRIUMF, and as a result is tightly integrated with the existing TIGRESS digital DAQ discussed in Ref. [12]. The decay time constant of the CsI ball preamplifiers discussed in Section 2.4 was set to 50 μs in order to obtain a count rate similar to that of

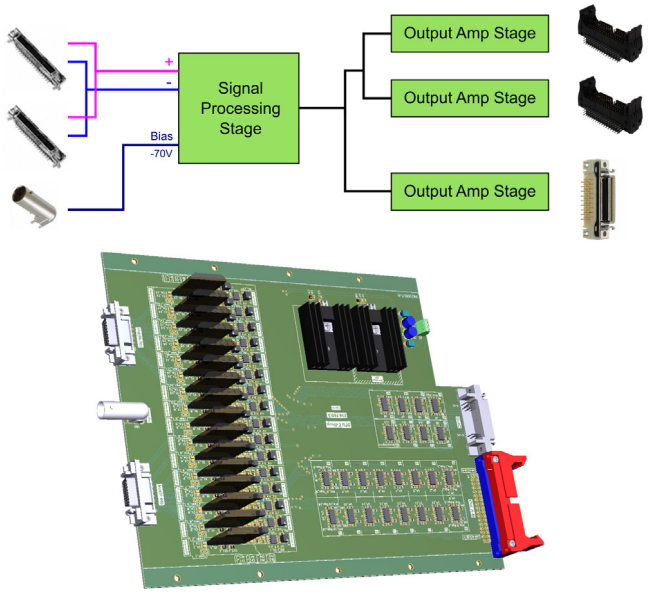

Fig. 5. Top: Block diagram of 16-fold preamplifier board developed at SFU for use with the CsI ball array. Bottom: Rendered image of board design.

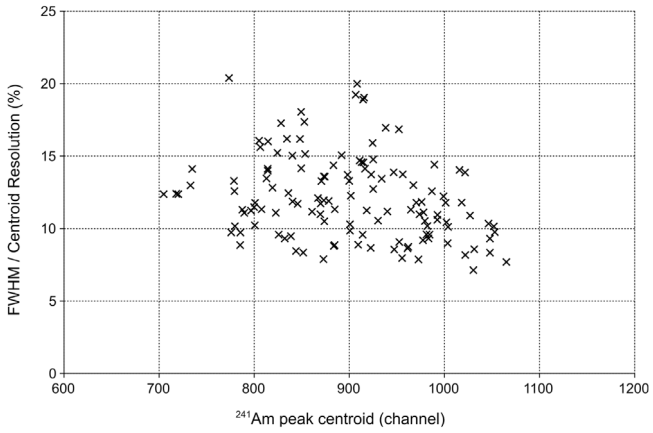

Fig. 6. Resolution and peak centroid of each of the 128 CsI ball array detectors. As all detectors were measured on the same preamplifier channel, the peak centroid represents a relative measure of light collection and photodiode response. Statistical uncertainties are on the order of 1 channel for the peak centroid values and 0.1% for the resolution values.

the TIGRESS array. This decay constant sets an upper limit on the rate of TIGRESS–CsI coincident events obtainable in an experiment without pileup. With a longer time constant the maximum CsI ball count rate would be reduced, possibly resulting in missed coincidences with TIGRESS. A shorter time constant would not be of practical benefit in this configuration, as the maximum rate of TIGRESS–CsI coincident events would still be limited by the TIGRESS count rate. Furthermore, the shorter time constant would result in increased distortion of the pulse shape, with some impact on the waveform fitting used for particle identification (PID). In particular, a longer time constant is preferable for experiments using radioactive beams. In that case, pileup is a lesser concern since the count rate is limited by the smaller beam currents available for species far from stability, and obtaining long undistorted waveforms is a higher priority.

Processed CsI(Tl) detector signals provided by the NIM preamplifier modules are passed to the TIGRESS digital DAQ, which is capable of evaluating complex trigger conditions containing signals from both detector arrays. Due to the slower timing response for CsI(Tl) scintillators compared to the HPGe clovers used in TIGRESS, a timing window on the order of 1 μs width must be used, causing some time-random background events to enter the data stream. Typical analysis of TIGRESS–CsI data includes separation of time correlated events, reducing this background contribution.

In the near future, the TIGRESS DAQ will be replaced by a system developed by the GRIFFIN collaboration at TRIUMF [13]. The increased data throughput provided by the GRIFFIN DAQ will allow for less complexity in the online trigger condition and will bias the event reconstruction procedure toward offline analysis. It will also be possible to increase the maximum count rate of the CsI ball by lowering the preamplifier time constant for future experiments in order to take advantage of the high data rate allowed by the GRIFFIN DAQ.

2.6. Detector testing

Signals from finished CsI ball detectors were verified using a ^{241}Am source, which emits alpha particles at 5485.56 and 5442.80 keV energy during its decay to ^{237}Np [14]. A source–detector distance of 51.7 mm was used for all detectors, which were tested individually using a common preamplifier channel, analog spectroscopy amplifier, and data acquisition system. Due to the intrinsic low energy resolution of CsI(Tl) detectors, a single peak was visible in the resulting energy spectra. Typical width/centroid resolution of the peak (used as a relative measure of signal quality) ranged from 7%–20% depending on the detector tested, with an average value of 12.1%. A plot of resolution and peak centroid values for each detector is shown in Fig. 6. The peak centroid represents a relative measure of the photodiode response of each individual detector, and is strongly affected by the light collection efficiency of the detector. Various factors can affect the resolution and light collection characteristics, including the geometry of the light guides (which depends on the detector ring) and/or optical imperfections in the interfaces between the CsI(Tl) crystal, light guide, and PIN diode.

3. Commissioning experiments

The CsI ball array was commissioned in a series of experiments at ISAC-II using TIP and TIGRESS in order to test its properties including particle detection efficiency and the ability to identify particles via waveform fitting. The charged particle detection efficiency of the CsI ball array was measured in two separate experiments, with the first employing a ^{196}Pt(α, α)^{196}Pt* Coulomb excitation reaction using a 2.0 mg/cm^2 enriched ^{196}Pt target and variable ^{4}He beam energy (see Section 3.1), and the second employing a ^{58}Ni(^{36}Ar, xpyn) fusion–evaporation reaction using an enriched 0.3 mg/cm^2 ^{58}Ni target and ^{36}Ar beam at 170 MeV (see Section 3.2). During the fusion–evaporation run, a 10.1 mg/cm^2 ^{181}Ta catcher foil was placed 2 mm downstream from the target to degrade the ^{36}Ar beam scattered into the CsI ball array. The individual detectors were also wrapped in lead absorber foils (shown in Fig. 3) during this group of experiments in order to stop any remaining ^{36}Ar beam. Absorber thicknesses used in these experiments allowed detection of alpha particles with energy ~6.5 MeV or higher, and protons ~3.6 MeV or higher. Absorber thicknesses and corresponding minimum detectable particle energies calculated using the ELAST [10] code are listed in Table 2. Due to the energy loss of charged particles in the absorbers, a charged particle energy calibration of the array can only be valid for the specific set of absorbers used in the same experiment, which is of importance for calorimetry experiments where good energy calibration is necessary in order to reconstruct the momenta of detected particles.

The aforementioned experiments were designed to allow for detection of alpha particles and protons in both the downstream and upstream rings of the CsI ball array, in order to obtain a good estimate of the charged particle efficiency of the full array. For this reason, experiments using inverse kinematics were avoided when commissioning the array. The charged particle efficiency of the array depends on both

Table 2
Lead absorber thicknesses used for each ring of the array and the associated transmission (Trans.) and detection (Det.) thresholds in MeV (calculated using the ELAST code [10]), assuming a 3 MeV minimum energy for charged particle detection. All energy values are in the lab frame.

Ring	Pb thickness (mg/cm^2)	p threshold		^{4}He threshold		^{36}Ar threshold	
		Trans.	Det.	Trans.	Det.	Trans.	Det.
0	18	1.38	3.70	5.38	7.25	94.5	129
1	17	1.32	3.67	5.15	7.05	86.5	122
2	17	1.32	3.67	5.15	7.05	86.5	122
3	16	1.26	3.63	4.92	6.85	78.5	114
4	16	1.26	3.63	4.92	6.85	78.5	114
5	16	1.26	3.63	4.92	6.85	78.5	114
6	15	1.20	3.59	4.67	6.65	70.4	106
7	15	1.20	3.59	4.67	6.65	70.3	106
8	14	1.14	3.56	4.42	6.44	62.5	97.6
9	14	1.14	3.56	4.42	6.44	62.5	97.6

the convolution of the array geometry shown in Section 2.1 with the angular distribution of charged particles, and the signal processing described in Sections 2.4 and 2.5, with the latter effect being independent of the reaction kinematics. The charged particle detection efficiency of the array for a reaction of interest can therefore be accurately predicted using simulations to determine a kinematic correction with respect to either of the reactions used to commission the array. To assist in experiment planning, kinematic corrections may be computed using GEANT4-based codes implementing fusion–evaporation and Coulomb excitation reaction processes, described in Refs. [6] and [7].

3.1. Coulomb excitation data analysis

In the Coulomb excitation experiment the data acquisition system was set to trigger upon single gamma-ray detection, and the efficiency of the CsI ball was taken as the ratio of the number of events containing a gamma ray at 355 keV corresponding to Coulomb excitation of ^{196}Pt and a hit in the CsI ball array to the number of events only containing a 355 keV gamma ray. The CsI ball array efficiency was measured at ^{4}He beam energies of 18.8, 14.6, and 10.2 MeV in order to determine the energy dependence of the detection efficiency for scattered alpha particles. Fig. 7 shows gamma-ray energy spectra obtained with and without the time coincidence condition for 18.8 MeV beam energy, using timing gate widths of 350 ns and 100 ns without background subtraction. As the ungated spectrum shown, lines from room background are unsuppressed when using a single gamma ray trigger, with a rate of 6.32(3) counts per second observed for the strongest line at 1461 keV from ^{40}K decay. The degree to which this time-random background is suppressed depends strongly on the timing gate width, and as such the contribution of time-random gamma rays at 355 keV affects the measured efficiency ϵ_{meas} as a function of the gate width. The true efficiency of the CsI ball array was determined under the assumption that the time-random background contribution to the efficiency is linear with gate width. This linear contribution was fitted and extrapolated, with the value at zero width representing the true efficiency ϵ_α in the absence of background.

3.2. Fusion–evaporation data analysis

In the fusion–evaporation experiment an online 2 particle — 2 Compton suppressed gamma ray trigger was used to separate background events from fusion–evaporation events. Channels observed at high intensity included ^{89}Mo and ^{89}Nb, corresponding to $4p1n$ and $5p$ evaporation from the compound nucleus ^{94}Pd, respectively. Fig. 8 shows the particle identification histogram obtained in this experiment, alongside an equivalent histogram for the Coulomb excitation experiment. Fig. 9 shows the gamma-ray spectra obtained from TIGRESS before and after gating on the $5p$ channel corresponding to ^{89}Nb. To avoid the need for Doppler correction of the data, stopped lines

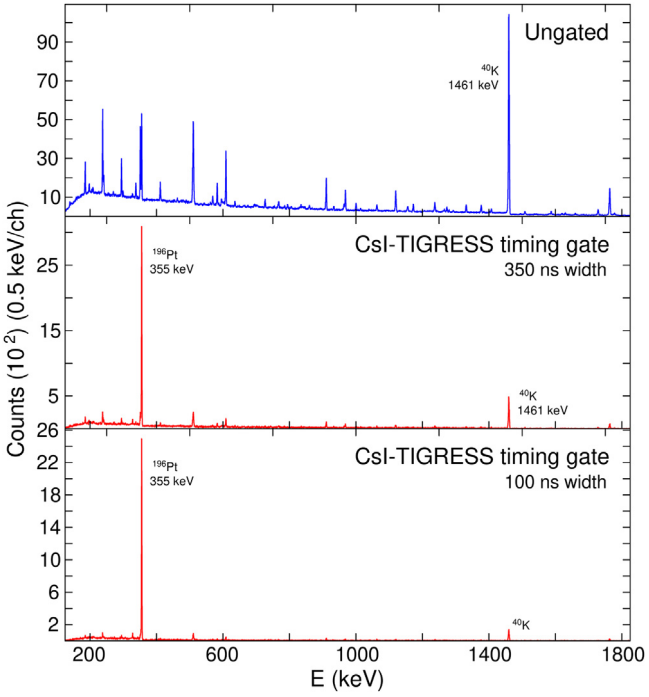

Fig. 7. Gamma-ray energy spectra from the Coulomb excitation experiment with 18.8 MeV ^{4}He beam energy, summed over TIGRESS detectors before (top) and after (bottom) gating on events in coincidence with a CsI ball hit, using 350 ns and 100 ns timing gate widths without background subtraction. The ^{40}K peak at 1461 keV represents a time-random background contribution in each spectrum, which is further quantified as a function of the timing gate width in Fig. 10.

corresponding to depopulation of isomers in ^{89}Mo and ^{89}Nb with $t_{1/2} \approx 1-10$ ns and their daughters were used in the subsequent analysis. These isomeric states decay after the nucleus of interest has been stopped in the ^{181}Ta catcher foil downstream of the target.

In the fusion–evaporation experiment, the proton detection efficiency ϵ_p of the CsI ball array was determined by examining gamma rays corresponding to known particle evaporation channels under different particle gating conditions. The number of counts observed for a specific transition under a specific particle gate depends on ϵ_p and a 'gating efficiency' ϵ_g which indicates the proportion of particles which are properly identified by the particle gate. For gamma rays belonging to the np evaporation channel, the number of counts $C_{n,x}$ in a given peak in the gamma-ray spectrum obtained when setting an xp gate is:

$$C_{n,x} = A_{n,x} \sum_{y=m}^{n} \binom{n}{y} \epsilon_p^y (1-\epsilon_p)^{n-y} \cdot \binom{y}{x} \epsilon_g^x (1-\epsilon_g)^{y-x}, \quad (1)$$

where m is the minimum number of particles detectable in a single event ($m \geq x$), and $A_{n,x}$ is a scaling factor. For the data presented here, a triggered event required detection of 2 particles, so $m \geq 2$. The two multiplicative terms of Eq. (1) indicate the probability of detecting y particles if n were emitted, and the probability of x particles falling into the particle gate if y were detected. In the case where $m = x$, the series in Eq. (1) simplifies to a single term:

$$C_{n,x} = A \binom{n}{x} \epsilon^x (1-\epsilon)^{n-x}, \quad (2)$$

where $\epsilon = \epsilon_p \epsilon_g$. A proof is given in Appendix A. Since Eq. (2) only contains the product of ϵ_p and ϵ_g, the values of ϵ_p and ϵ_g cannot be uniquely determined under the condition $m = x$, where Eq. (2) is valid. Therefore data with $m > x$ ($x < 2$) was examined to determine the proton and gating efficiency. A χ^2 minimization was performed to

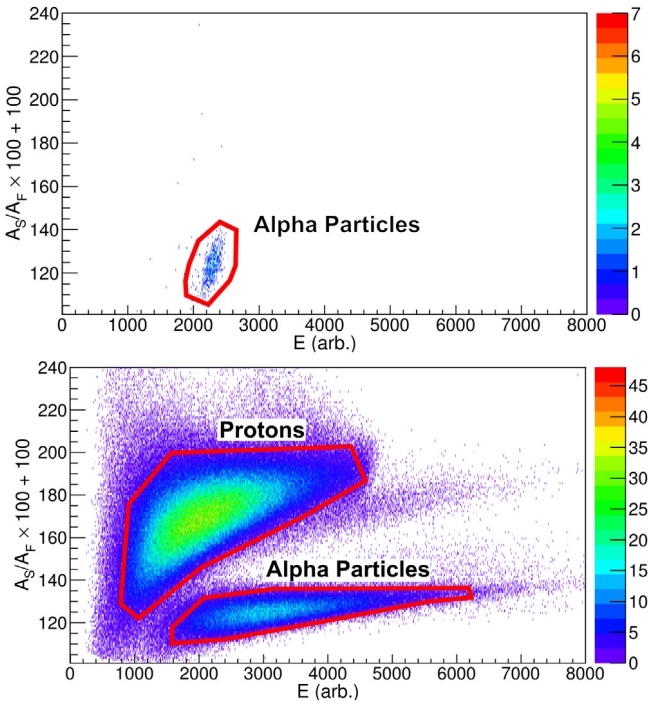

Fig. 8. Particle identification (PID) histograms for a ring 3 detector from the ^{196}Pt(α, α)^{196}Pt* Coulomb excitation experiment (top) and the ^{58}Ni(^{36}Ar, x) fusion–evaporation experiment (bottom), with particle gates drawn over top. A_S and A_F refer to the slow and fast components of the pulse shape, as defined in Ref. [1]. Features outside of the particle gates do not have sufficient statistics to be rigorously identified.

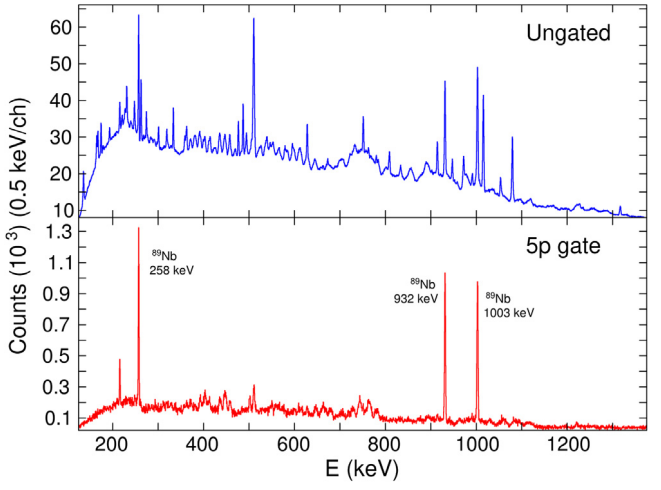

Fig. 9. Gamma-ray energy spectra summed over TIGRESS detectors before (top) and after (bottom) gating on events in coincidence with 5 protons. Following gating, the ^{58}Ni(^{36}Ar,5p)^{89}Nb reaction channel is isolated. Data is not Doppler corrected, stopped peaks correspond to depopulation of long-lived isomers and their daughter states.

determine the global best fit values of $A_{n,x}$, ϵ_p, and ϵ_g:

$$\chi^2 = \sum_{n,x} \left(\frac{O_{n,x} - C_{n,x}}{\sigma_{O_{n,x}}} \right)^2, \tag{3}$$

where $O_{n,x}$ is the observed number of counts in a peak of interest belonging to the np channel when setting an xp gate on the experimental data, with 1σ uncertainty $\sigma_{O_{n,x}}$ determined from the peak fit.

Table 3
Measured alpha particle detection efficiencies ϵ_α for the CsI ball array in the ^{196}Pt Coulomb excitation experiment.

^{4}He energy (MeV)	ϵ_α
18.8	0.688(4)
14.6	0.65(1)
10.2	0.566(1)

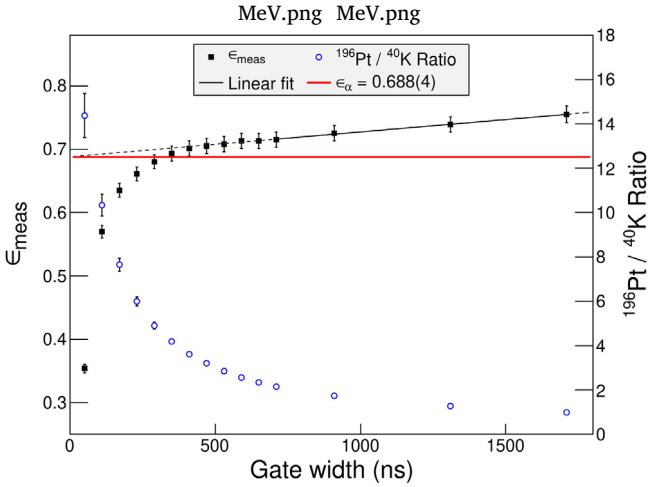

Fig. 10. Measured efficiency ϵ_{meas} of the CsI ball array in the ^{196}Pt Coulomb excitation experiment with 18.8 MeV ^{4}He beam energy, as a function of timing gate width. The true alpha efficiency ϵ_α is obtained by extrapolating the linear background contribution to zero gate width (extrapolation outside of the fit region is indicated by a dashed line). The ratio of counts in the 355 keV (from ^{196}Pt Coulomb excitation) and 1461 keV (from ^{40}K decay) peaks is also plotted as an indication of the signal-to-background ratio.

4. Results

Table 3 lists alpha particle detection efficiencies ϵ_α for the CsI ball array obtained in the ^{196}Pt Coulomb excitation experiment as a function of ^{4}He beam energy. As is further discussed in Section 5, the extracted alpha particle detection efficiency has a clear energy dependence, with larger values obtained at higher beam energies. Fig. 10 shows the extraction of ϵ_α for the data corresponding to 18.8 MeV ^{4}He beam energy.

Also shown in Fig. 10 is the ratio of counts in the 355 keV peak from ^{196}Pt Coulomb excitation to the background line at 1461 keV as a function of timing gate width. It is evident that smaller gate widths result in increased background suppression at the expense of detection efficiency for time coincident events. Wider gate widths may be used to increase this efficiency, however as shown in Fig. 10 for widths larger than 400 ns any further increase in the number of counts in the 355 keV peak results entirely from random background events with the desired energy rather than true time coincidences. Using the fractional uncertainty of the number of true time coincidences as a figure of merit, an optimal gate width of 350 ns is obtained for TIGRESS–CsI ball timing (see Appendix C). This optimal gate width is significantly longer than the digitization time of the TIGRESS DAQ (10 ns), and results from the time resolution of the individual detection systems and signal processing. The aforementioned figure of merit may not necessarily be suitable for all experiments — as Fig. 7 shows, the signal-to-background ratio is improved for gate widths shorter than 350 ns at the expense of detection efficiency. In experiments where suppression of background is a priority, a narrower gate width below 200 ns may be preferable to obtain a superior signal-to-background ratio.

The proton detection efficiency parameters determined in the ^{58}Ni(^{36}Ar, xpyn) fusion–evaporation experiment via minimization of

Table 4
Measured proton detection and gating efficiencies for the CsI ball array in the ^{58}Ni(^{36}Ar, xp) fusion–evaporation experiment.

Quantity	Value
ϵ_p	0.635(2)
ϵ_{gate}	0.909(2)

the χ^2 defined in Eq. (3) are reported in Table 4. Fig. 11 shows the global fit to the data. The goodness-of-fit statistic was $\chi^2/\nu = 5.22$, indicating some underestimation of counting errors in the gated spectra. This can result from overcounting due to the presence of background peaks from other channels with similar energy to the peak of interest. However as indicated in Table 4 the efficiency parameters were well constrained by the fit.

5. Discussion

The charged particle detection efficiencies $\epsilon_\alpha = 0.688(4)$ and $\epsilon_p = 0.635(2)$ measured in the two experiments vary in part due to the differences in reaction kinematics. In particular, the thermal distribution of particle energies following fusion–evaporation reactions will always contain a fraction of particles below the detection threshold, which negatively impacts the detection efficiency.

The effect of the particle energy distribution on the proton detection efficiency was investigated using the GEANT4-based code described in Ref. [6] to simulate the ^{58}Ni(^{36}Ar,4p)^{90}Mo reaction incorporating realistic geometry for the ^{58}Ni target, TIGRESS, and the CsI ball array. Using the proton center-of-mass energy distribution obtained for this reaction from the PACE4 code [15] and no energy threshold for proton detection, a proton efficiency $\epsilon_g = 0.9682(1)$ was obtained from the GEANT4 simulations based on the geometry of the target (with appropriate target thickness and density, but no target holder) and the detector arrays. When using a 3.56 MeV proton detection threshold (the lowest detectable proton energy from Table 2), a reduced geometric proton efficiency $\epsilon_{g,red} = 0.8920(3)$ was obtained, a reduction of 7.6% compared to the full geometric efficiency. The observed efficiency $\epsilon_p = 0.635(2)$ is approximately 71% of this reduced geometric efficiency. A large contribution to this difference is shadowing from the TIP target holder. In the configuration used during the commissioning experiments, the target holder geometry shadows the angular range $82.6° \leq \theta \leq 102.8°$. When incorporating this shadow into the GEANT4 simulations (by vetoing detection of charged particles emitted at angles within the shadow) along with the proton detection threshold, a realistic simulated efficiency $\epsilon_{sim} = 0.7425(6)$ is obtained and the observed efficiency is 85% of this simulated efficiency. The remaining 15% difference is understood to arise from losses incurred during data acquisition and signal processing.

Simulations were also performed for the Coulomb excitation experiments using GEANT4 code described in Ref. [7], using the target holder shadow correction and an alpha particle detection threshold of 6.44 MeV. For the data using 18.8 MeV alpha particles, the ratio of observed and simulated efficiencies was approximately 85%, consistent with the fusion–evaporation experiment. This consistency between simulations of different experimental conditions indicates that the charged particle efficiency of the array can be predicted for arbitrary reactions of interest. However, the GEANT4 simulations further over-predict the array efficiency for the Coulomb excitation data using lower alpha particle energies of 14.6 and 10.2 MeV. These alpha particles were well above the energy thresholds listed in Table 2, indicating that this effect is not related to the detection threshold resulting from energy loss in the absorbers. The reduction of charged particle detection efficiency due to data acquisition and signal processing is therefore energy dependent, with approximately 15% reduction in efficiency for charged particles far above the detection threshold, and 30% or larger reduction in efficiency for charged particles near the detection threshold, as shown in Table 5. This effect arises from a combination of factors including the time response of the CsI(Tl) scintillators (particularly time walk as a function of signal amplitude) and the communication latency between DAQ subsystems.

Table 5
Comparison of CsI ball charged particle detection efficiencies obtained from the experiments described in Section 3 and the GEANT4 simulations described in Refs. [6] and [7]. Simulated efficiencies ϵ_{sim} were computed using a correction for the TIP target and using proton and alpha particle energy thresholds of 3.56 and 6.44 MeV, respectively (taken from Table 2).

Reaction	ϵ_{expt}	ϵ_{sim}	$\epsilon_{expt}/\epsilon_{sim}$
^{58}Ni +^{36}Ar fusion–evaporation	0.635(2)	0.7425(6)	0.855(3)
^{196}Pt Coulex, $E_\alpha = 18.8$ MeV	0.688(4)	0.8190(13)	0.840(5)
^{196}Pt Coulex, $E_\alpha = 14.6$ MeV	0.65(1)	0.817(3)	0.795(13)
^{196}Pt Coulex, $E_\alpha = 10.2$ MeV	0.566(1)	0.8078(18)	0.6908(19)

For the purposes of planning experiments, it is advisable that raw simulated efficiencies based on the array geometry and detection thresholds be reduced by a factor of 20% for intermediate energy (10–15 MeV) and 15% for high energy (> 15 MeV) charged particles, to obtain a realistic estimate which takes all of the aforementioned effects into account.

In summary, the TIP CsI ball array has been built and commissioned at SFU and TRIUMF. Future planned experiments with the array include studies of proton rich $N = Z$ nuclei using fusion–evaporation reactions on ^{40}Ca targets, as well as studies of neutron rich species produced in fusion–evaporation reactions via proton gating. When combined with plunger lifetime measurements utilizing radioactive beams available at TRIUMF/ISAC-II and the upcoming TRIUMF/ARIEL facility, the CsI ball array will provide a unique opportunity for high precision transition strength measurements in nuclei far from stability.

Acknowledgments

The authors would like to acknowledge the support of the ISAC Operations Group and Detector Group at TRIUMF, and the Simon Fraser University Electronics and Machine Shops.

This work was supported by the Natural Sciences and Engineering Research Council of Canada, the Canadian Foundation for Innovation and the British Columbia Knowledge Development Fund. TRIUMF receives federal funding through a contribution agreement with the National Research Council of Canada.

The authors would like to acknowledge the contributions of R. A. E. Austin and J. J. Ressler to this project.

Appendix A. Particle gating combinatorics

Take the special case of Eq. (1) where $m = x$:

$$C_{n,x} = A_{n,x} \sum_{y=x}^{n} \binom{n}{y} \epsilon_p^y (1-\epsilon_p)^{n-y} \cdot \binom{y}{x} \epsilon_g^x (1-\epsilon_g)^{y-x}. \tag{A.1}$$

The binomial coefficients may be combined:

$$\begin{aligned} \binom{n}{y}\binom{y}{x} &= \frac{n!}{y!(n-y)!} \cdot \frac{y!}{x!(y-x)!} \\ &= \frac{n!}{x!(n-x)!} \cdot \frac{(n-x)!}{(n-y)!(y-x)!} \\ &= \binom{n}{x}\binom{n-x}{y-x}. \end{aligned} \tag{A.2}$$

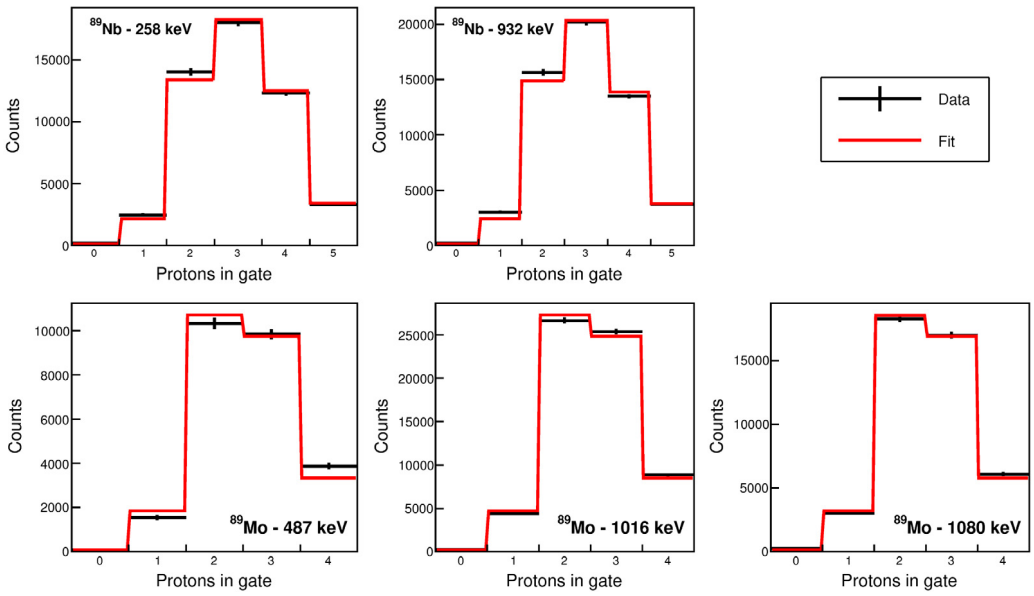

Fig. 11. Eq. (1) fitted to fusion–evaporation data for various transitions in ^{89}Nb and ^{89}Mo, as a function of the number of particles in the proton gate x.

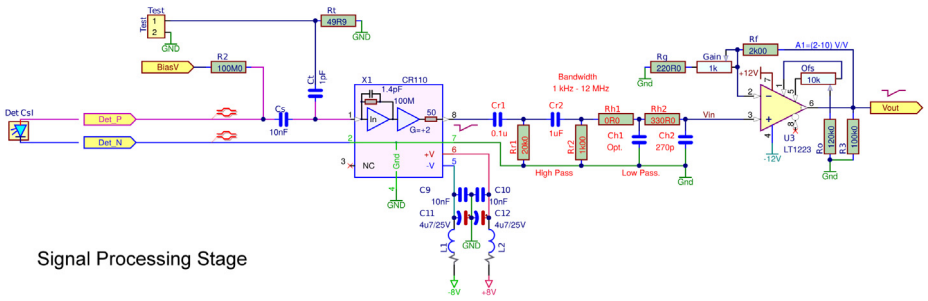

Fig. B.1. Schematic of signal processing stage of CsI ball array preamplifier boards. From left to right: the raw signal is passed through a CR-110 charge sensitive preamplifier module, high pass and low pass filters for noise reduction, and is amplified prior to output.

Eq. (A.1) may then be written:

$$\begin{aligned} C_{n,x} =& A_{n,x} \sum_{y=x}^{n} \binom{n}{x}\binom{n-x}{y-x} \epsilon_p^y \epsilon_g^x \\ & (1-\epsilon_p)^{n-y}(1-\epsilon_g)^{y-x} \\ =& A_{n,x}\binom{n}{x}\epsilon^x \sum_{y=x}^{n}\binom{n-x}{y-x}(1-\epsilon_p)^{n-y} \\ & \epsilon_p^{y-x}(1-\epsilon_g)^{y-x}. \end{aligned} \tag{A.3}$$

where $\epsilon = \epsilon_p\epsilon_g$. From the binomial theorem:

$$\sum_{i=0}^{j}\binom{j}{i}a^{j-i}b^i = (a+b)^j. \tag{A.4}$$

substituting $i = y - x$, $j = n - x$ with $j - i = n - y$, $a = 1 - \epsilon_p$, and $b = \epsilon_p(1-\epsilon_g)$, Eq. (A.3) may be re-written:

$$\begin{aligned} C_{n,x} &= A_{n,x}\binom{n}{x}\epsilon^x(1-\epsilon_p+\epsilon_p-\epsilon_p\epsilon_g)^{n-x} \\ &= A\binom{n}{x}\epsilon^x(1-\epsilon)^{n-x}. \end{aligned} \tag{A.5}$$

Hence the sum of Eq. (1) collapses to a single term under the condition $m = x$.

Appendix B. Preamplifier signal processing stage

Fig. B.1 shows a detailed schematic of the signal processing stage used in the CsI ball preamplifier boards.

Appendix C. Figure of merit for timing gate

The optimal TIGRESS–CsI ball timing gate width was chosen as the width for which the fractional uncertainty $\Delta C/C$ on the number of true time-correlated events C is minimized. The total number of events T falling within a time coincidence gate is the sum of events corresponding to true coincidences C and random background events B, therefore:

$$\begin{aligned} C &= T - B \\ \Delta C &= \sqrt{(\Delta T)^2 + (\Delta B)^2}. \end{aligned} \tag{C.1}$$

The number of random background events B is not directly measured, but may be calculated:

$$B = m \cdot t_{gate}, \tag{C.2}$$

where m is the number of random background events which are observed per unit gate width, and t_{gate} is the timing gate width. Assuming that the time-random background contribution to the count rate is linear with gate width, the value of m may be extracted by fitting this linear contribution as shown in Fig. C.1 (similar to the fit shown in Fig. 10). From the slope of the fit line, the best fit value of m was determined to be $6.9(4) \times 10^{-1}$ ns^{-1} for the TIGRESS–CsI ball system (i.e. $\Delta m = 0.4 \times 10^{-1}$ ns^{-1}).

The error on the total number of counts ΔT was directly extracted from the data, and the error on the number of uncorrelated events $\Delta B = \Delta m \cdot t_{gate}$ was calculated to obtain the uncertainty on the number of correlated events ΔC using Eq. (C.1). The minimum value of the

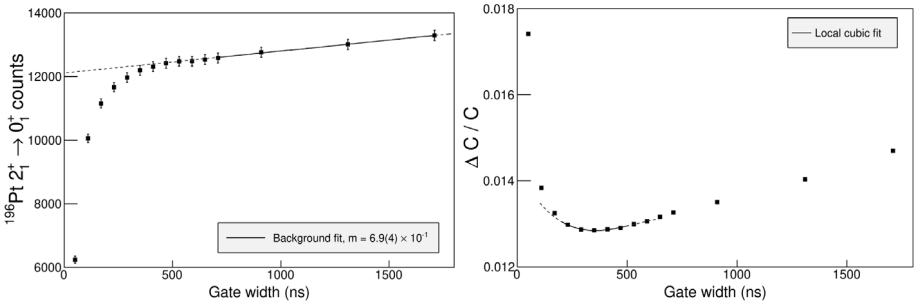

Fig. C.1. Left: Measured total number of events T in the 355 keV gamma ray from ^{196}Pt Coulomb excitation. The fitted line shows the time-random background contribution to the observed peak, similar to Fig. 10. Right: The timing gate figure-of-merit $\Delta C/C$ as a function of gate width. A cubic fit function is shown with a local minimum at t_{gate} = 354 ns. In both plots, dashed lines indicate extrapolation of fit functions beyond the fitting range.

fractional uncertainty $\Delta C/C$ was used to determine the optimal timing gate width of approximately 350 ns, as shown in Fig. C.1.

References

[1] P. Voss, et al., The TIGRESS integrated plunger ancillary systems for electromagnetic transition rate studies at TRIUMF, Nucl. Instrum. Methods Phys. Res. A 746 (2014) 87–97.
[2] G. Hackman, C.E. Svensson, The TRIUMF-ISAC gamma-ray escape suppressed specrometer, TIGRESS, Hyperfine Interact. 225 (1) (2014) 241–251.
[3] R.E. Laxdal, Acceleration of radioactive ions, Nucl. Instrum. Methods Phys. Res. B 204 (2003) 400–409.
[4] K.W. Allen, Doppler shift timing methods, in: The Electromagnetic Interaction in Nuclear Spectroscopy, North-Holland Publishing Company, 1975, pp. 311–339.
[5] A. Dewald, O. Möller, P. Petkov, Developing the recoil distance Doppler-shift technique towards a versatile tool for lifetime measurements of excited nuclear states, Prog. Part. Nucl. Phys. 67 (2012) 786–839.
[6] J. Williams, et al., Implementation of the Doppler shift attenuation method using TIP/TIGRESS at TRIUMF: Fusion-evaporation lifetime measurements in ^{22}Ne, Nucl. Instrum. Methods Phys. Res. A 859 (2017) 8–17.
[7] A. Chester, et al., Recoil distance method lifetime measurements at TRIUMF-ISAC using the TIGRESS integrated plunger, Nucl. Instrum. Methods Phys. Res. A 882 (2018) 69–83.
[8] A. Chester, et al., Recoil distance method lifetime measurement of the 2_1^+ state in ^{94}Sr and implications for the structure of neutron-rich Sr isotopes, Phys. Rev. C 96 (2017) 011302(R).
[9] D.G. Sarantites, et al., The Microball: Design instrumentation and response characteristics of a 4p-multidetector exit channel-selection device for spectroscopic and reaction mechanism studies with gammasphere, Nucl. Instrum. Methods Phys. Res. A 381 (1996) 418–432.
[10] Energy Loss And Straggling Tool (ELAST). Based on ENELOSS, written by H. Ernst (1981) with stopping power routines by K. Lesko (1984).
[11] http://www.cremat.com/. (Accessed 18 September 2018).
[12] J.-P. Martin, et al., The TIGRESS DAQ/trigger system, IEEE Trans. Nucl. Sci. 55 (1) (2008) 84–90.
[13] A.B. Garnsworthy, et al., The GRIFFIN data acquisition system, Nucl. Instrum. Methods Phys. Res. A 853 (2017) 85–104.
[14] M.S. Basunia, Nuclear data sheets for A = 237, Nucl. Data Sheets 107 (2006) 2323–2422.
[15] A. Gavron, Statistical model calculations in heavy ion reactions, Phys. Rev. C 21 (1) (1980) 230–236.